PHYSICAL REVIEW B VOLUME 43, NUMBER 8 15 MARCH 1991-I

Correlation of hot-phonon and hot-carrier kinetics in Ge on a picosecond time scale

Andreas Othonos and H. M. van Driel
Department of Physics, University of Toronto and Ontario Laser and Lightwave Research Centre, Toronto Canada, M5S 1A7

Jeff F. Young and Paul J. Kelly
Division of Physics, National Research Council, Ottawa Canda, K1A 0R6
(Received 9 May 1990; revised manuscript received 7 December 1990)

We report room-temperature measurements of time-resolved reflectivity from intrinsic crystalline Ge induced and probed by $\lambda=0.575$ μm, 2-ps pulses and for photogenerated carrier densities up to $\sim 10^{19}$ cm^{-3}. These data are used together with our earlier picosecond-time-resolved Raman-scattering data at 77 and 300 K to self-consistently determine transient nonequilibrium carrier and phonon effects. The combined data sets are modeled with a Boltzmann transport description of coupled electron and phonon kinetics to understand the temporal and spatial evolution of carrier density and temperature and the generation and decay of Raman-active phonons. Using known material parameters in the model, we can account for the magnitude and temporal evolution of the electron, hole, and phonon thermodynamic parameters. In particular, the model accounts for the relative delay between the peak of the pulse and the nonequilibrium phonon population, the number of nonequilibrium phonons generated, and the initially rapid diffusion of hot carriers away from the sample surface on a 5-ps time scale.

I. INTRODUCTION

Over the last few years many experiments in semiconductors have separately probed aspects of hot-carrier and phonon dynamics on a picosecond or subpicosecond time scale using ultrashort light pulses.[1-12] At very high peak intensities the electron and hole subsystems can be driven far out of equilibrium as can certain phonon modes. Although much of the emphasis has been on understanding nonequilibrium carrier kinetics alone, it is generally realized that nonequilibrium phonon effects can influence hot-carrier relaxation and transport.[13,14] In fact, observations of nonequilibrium phonon populations through transient Raman scattering[8-12] have directly provided evidence for the existence and decay of nonequilibrium phonon populations generated by hot-carrier relaxation. However, there has been extremely little work directed towards studying *both* the carrier and the phonon dynamics under experimental conditions that can be related to a single, self-consistent theoretical model. Clearly we will improve our understanding of subtle aspects of the coupled system dynamics if we can correlate the behavior of carrier and phonon systems. This paper reports on our efforts to achieve this for intrinsic crystalline germanium at $T=77$ and 300 K.

Germanium might seem an unlikely candidate for such a study given the fact that relatively little research has been performed on group-IV, as compared to group-III-V materials, with respect to aspects of hot-carrier and phonon dynamics. Progress in understanding the details of hot-carrier relaxation in group-IV semiconductors has not advanced at the same pace as in group III-V materials due largely to the indirect band gaps of Si and Ge. Experimental techniques such as time-resolved photoluminescence and differential absorption spectroscopies that have proved so powerful in the III-V materials are limited in their utility when the fundamental gap is indirect. Transient transmission, reflection, and diffraction measurements have been carried out for Ge and Si, but most of this work was concerned with high excitation levels where nonlinear absorption and recombination processes often obscure the more subtle carrier-lattice interactions. It is only recently that transient Raman-scattering[11,12] experiments have been done at sufficiently low injected-carrier densities to make use of detailed microscopic models of the energy relaxation processes.

Despite this relative lack of work on group-IV materials, the fact that they are centrosymmetric gives them a tremendous advantage over their noncentrosymmetric group III-V counterparts if one explicitly wishes to study both carrier and lattice dynamics under comparable experimental conditions. This is so because the longitudinal-optic-phonon modes in centrosymmetric material generate no macroscopic electric field and hence they do not couple with long-range electric fields associated with free-carrier density fluctuations. This has the practical consequence that the Raman-active optical phonons in Ge do not become renormalized in the presence of free carriers due to plasmon-phonon coupling, so that they may be observed, unaltered, up to densities of $\sim 10^{20}$ cm^{-3}. The lack of long-range coupling between optical phonons and free carriers also tremendously simplifies the microscopic modeling of carrier-phonon dynamics, since many-body effects can be ignored to first order. Although many models of hot-carrier dynamics in group III-V materials also ignore many-body effects, the problem there is manifestly many-body in nature, and any truly complete understanding will eventually have to treat the many-body-related issues. In addition to these technical reasons for studying Ge, there is also a practical

 ©1991 The American Physical Society

motivation for developing techniques to address these issues in group-IV materials since sophisticated, high-speed electronic devices such as double-barrier resonant tunneling structures are now being studied in the Si/Si-Ge material system.[15]

We have carried out studies using picosecond Raman scattering and visible reflectivity measurements in conjunction with a self-consistent kinetic model for investigating nonequilibrium carrier and phonon dynamics, In the experiments, moderate excitation levels are used for which minimal lattice heating occurs and for which nonlinear absorption and recombination processes, which complicate the analysis of high-excitation experiments in Ge or Si, are also absent. This allows a detailed analysis of the results using a model which focuses on the microscopic energy relaxation processes, in much the same way as is commonly done for III-V materials.

One important result of this study is the achievement of quantitative agreement between theory and experiment for the absolute nonequilibrium optical-phonon population generated (~ 0.1) at an injected-carrier density of $\sim 10^{18}$ cm^{-3}. Such a large nonequilibrium population demonstrates that even with a wave vector independent carrier-phonon matrix element, as is appropriate for the deformation-potential interactions in Ge, pure kinematic constraints of energy and momentum conservation severely limit the range of wave vectors through which energy may be transferred to the lattice from the hot carriers. Another interesting effect, predicted by the model and verified by a time-resolved reflectivity experiment, is the very significant role played by the carrier temperature dependence of the carrier diffusion coefficient, even on picosecond time scales. This temperature dependence leads to enhanced diffusion during and shortly after the optical pulse.

In Sec. II we briefly review the different experimental methods. Section III contains a detailed description of the theoretical model, which includes assumptions for the band-gap structure, transport equations for carrier density and temperatures, and the various energy-loss mechanisms. In Sec. IV we describe our experimental results and compare them with numerical solutions of our model for $\lambda = 0.575$ μm picosecond laser pulse excitation. Inclusion of optical-phonon generation in the model allows us to calculate the nonequilibrium optical-phonon populations and compare them with values obtained from transient Raman scattering. From the analysis of the carrier profiles obtained from the simulations we also demonstrate that a simple Drude model is sufficient to explain the time-resolved reflectivity measurements.

II. EXPERIMENTAL DETAILS

The experimental setup used to time resolve the anti-Stokes component of the Raman signal from nonequilibrium optical phonons in Ge has been described in detail elsewhere.[11] Briefly, pump and perpendicularly polarized probe beams were derived from a train of 4-ps [full width at half maximum (FWHM)] 76 MHz synchronously mode locked pulses at 0.575 μm. The pump pulses were focused to yield a fluence (F) of ~ 0.1 mJ/cm^2 per pulse on ~ 2-mm-thick crystalline Ge [001] and [110] surfaces while the probe pulses were focused to the same spot size, with $\sim 30\%$ of the pump beam's fluence. Scattered light due to the probe beam was collected in a backscattering geometry and the anti-Stokes component was monitored on a silicon charge-coupled array detector at the output of a triple spectrograph. Raman selection rules dictate that only LO phonons, on [100] surfaces, and TO phonons, on [110] surfaces, can be observed in first-order backscattering spectra.

The time-resolved reflectivity measurements were performed using two different experimental arrangements, with similar results being obtained. First, pulses of 6 ps (FWHM) duration from a synchronously pumped $\lambda = 0.575$ μm dye laser were amplified with a four-stage dye cell system, pumped at 20 Hz by an excimer laser.[16] The amplified pulses were split into orthogonally polarized pump and probe beams and then superimposed on a 2-mm-thick [100] Ge sample. A 10° angle between pump and probe pulses was used with the probe beam focused to one fifth of the pump beam diameter. The peak fluence of the pump pulse was 5 mJ/cm^2 in a spot of 1 mm diameter. In the second experiment the 2 ps pump and probe beams were derived from a synchronously pumped dye laser with a cavity dumper operating at 3.8 MHz. The pump pulses were focused at normal incidence to a fluence of $F \approx$ mJ/cm^2 in a 50 μm diam spot while the probe pulses, incident at a 15° angle with respect to the normal, were focused to one-fifth this spot size at a fluence of ≤ 20 μJ/cm^2. The high repetition rate permitted lock-in detection for data collection, yielding an improved signal-to-noise ratio over that obtained from the boxcar detection scheme used with the amplified pulses. Only the results from this experiment will be reported here.

The sample temperature in the Raman experiments was 77 or 300 K while for the reflectivity experiments reasonable signal-to-noise ratios could only be achieved for 300 K. All samples used were intrinsic specimens.

III. THEORETICAL MODEL

The fundamental interactions which occur during and following the absorption of picosecond, above-band-gap laser pulses in a semiconductor have been described by many authors.[17,18] Here we give a brief summary of the processes that are relevant to our work and the necessary considerations to incorporate nonequilibrium phonon effects.

Germanium is an indirect-gap semiconductor with a highly anisotropic and complex band structure.[19] To make our calculations tractable, we have made simplifying assumptions about the band structure similar to those described by Elci *et al.*[18] In particular, in the conduction band we assume that the band-edge energies of the 4 L and 6 X valleys are the same, but assign each their respective effective masses. In the valence band the split-off band is neglected due to its small density of states. Heavy and light holes are considered degenerate since at the elevated temperatures of interest here, the curvatures of the two valence bands are identical, and

there is very little difference in their energies.

The model allows for one- and two-photon interband absorption and single-photon free-carrier absorption. However, for the excitation levels used in the experiments, the dominant absorption mechanism is single-photon interband absorption near the Γ point of the Brillouin zone. This results in the creation of electron-hole pairs with total kinetic energy $\hbar\omega - E_g$. The electrons initially created in the Γ valley quickly scatter into the side valleys, where they are assumed to establish a Maxwell-Boltzmann distribution through electron-electron scattering with an initial temperature, i.e., in the absence of cooling, of ~6800 K (at an ambient temperature of 77 K). Once in the side valleys the hot electrons thermalize with the lattice via electron-phonon deformation-potential interactions, and with the cooler holes (initial hole temperature ~3000 K at an ambient temperature of 77 K) via the Coulomb interaction. The intraband optical-phonon mediated relaxation of L-valley electrons (X valley forbidden) and heavy holes generates nonequilibrium populations of optical phonons with relatively small wave vector which can be monitored via Raman scattering. Energy relaxation via acoustic-mode phonons and intervalley optical phonons also contributes to cooling of the carriers, but without generating any small wave-vector optical phonons, which can be probed by Raman scattering with visible light.

To model the dynamics of hot electrons, holes, and optical phonons, we use the formalism of van Driel[17] which deals with coupled Boltzmann's equations, in the relaxation time approximation, for particle number, particle energy, and lattice energy. In his model three coupled continuity equations are solved numerically for the depth and time-dependent carrier density N, carrier temperature T_c (the subscript c will signify carriers $\equiv e,h$) and lattice temperature T_L. To specifically model the Raman and reflectivity experiments in Ge, van Driel's formalism was generalized to include different electron and hole temperatures, and to include detailed microscopic expressions for energy exchange processes between carriers and phonons. The modified model therefore involves the solution of four coupled differential equations for the spatial and temporal dependence of N, T_e, T_h, and T_L. From these parameters and the microscopic model of the carrier-phonon interaction one can also obtain the time evolution of the population $(n_{\mathbf{q}})$ of the appropriate Raman-active phonons of wave vector $\mathbf{q}$.

Following van Driel, one can proceed from the microscopic Boltzmann equation to a macroscopic description by integrating the microscopic transport quantities over the appropriate carrier or phonon distribution functions. In the relaxation time approximation of Boltzmann's equation one obtains relations for the electrical $(\mathbf{j}_c)$ and energy current $(\mathbf{W}_c)$ of the carriers

$$\mathbf{j}_c = \frac{1}{e}\sigma_c \nabla \xi_c - \sigma_c Q_c \nabla T_c \ , \tag{1}$$

$$\mathbf{W}_c = \left[\Pi_c - \frac{\xi_c}{e} \right] \mathbf{j}_c - \kappa_c \nabla T_c \ , \tag{2}$$

where σ_c is the electrical conductivity, Q_c is the Seebeck coefficient, Π_c is the Peltier coefficient, κ_c is the thermal conductivity, $-e$ is the charge of an electron, and ξ_c is the chemical potential of the carriers. For an intrinsic semiconductor under laser excitation, phonon scattering is expected to be the most important mechanism involving free carriers. This implies that the energy dependence[20] of the momentum relaxation is proportional to $(E-E_c)^{-1/2}$. Under these assumptions the coefficients in Eqs. (1) and (2) are given by

$$\begin{aligned} &\sigma_c = eN\mu_{\rm MB}^c \mathcal{H}_{1/2}^0(\eta_c), \quad Q_c = -\frac{k_B}{e_c}[\eta_c - 2\mathcal{H}_0^1(\eta_c)] \ , \\ &\Pi_c = -T_c \frac{k_B}{e_c}[\eta_c - 2\mathcal{H}_0^1(\eta_c)] \ , \\ &\kappa_c = \frac{k_B^2 \sigma_c T_c}{e^2}\{6\mathcal{H}_0^2(\eta_c) - 4[\mathcal{H}_0^1(\eta_c)]^2\} \ , \end{aligned} \tag{3}$$

where $\mathcal{H}_j^i(\eta_c)$ is the ratio of the Fermi-Dirac integrals $\mathcal{F}_i(\eta_c)/\mathcal{F}_j(\eta_c)$ for reduced Fermi-level η_c, and $\mu_{\rm MB}^c$ is the mobility of carriers in a Maxwell-Boltzmann distribution and, e_c equals $-e$ for electrons and $+e$ for holes. For a laser-induced plasma the Dember field which develops due to charge separation prohibits the carrier charge and current density from becoming significantly different so that

$$\mathbf{j}_e = -\mathbf{j}_h, \quad N = N_e = N_h \ . \tag{4}$$

From the above equations we can write the particle current $\mathbf{J} = -\mathbf{j}_e/e$ as follows:

$$\mathbf{J} = -D\left[\nabla N + \frac{N}{k_B T_{eh}}\nabla E_g + \frac{N}{T_{eh}}[\mathcal{H}(\eta_e)\nabla T_e + \mathcal{H}(\eta_h)\nabla T_h]\right] \ , \tag{5}$$

where $T_{eh} = T_e \mathcal{H}_{-1/2}^{1/2}(\eta_e) + T_h \mathcal{H}_{-1/2}^{1/2}(\eta_h)$, $\mathcal{H}(\eta_c) = 2\mathcal{H}_0^1(\eta_c) - \frac{3}{2}\mathcal{H}_{-1/2}^{1/2}(\eta_c)$, $E_g = E_C - E_V$ is the band-gap energy, and the ambipolar diffusion coefficient D is given by

$$D = D_e^0 D_h^0 \frac{T_e \mathcal{H}_{-1/2}^{1/2}(\eta_e) + T_h \mathcal{H}_{-1/2}^{1/2}(\eta_h)}{D_h^0 T_e \mathcal{H}_0^{1/2}(\eta_e) + D_e^0 T_h \mathcal{H}_0^{1/2}(\eta_h)} \ . \tag{6}$$

$D_e^0 \propto T_e^{1/2}$, $D_h^0 \propto T_h^{1/2}$ are the low-density electron and hole diffusion constants appropriate for the ambient lattice temperature. The energy current for electrons and holes can be rewritten in the following form:

$$\begin{aligned} &\mathbf{W}_e = \mathbf{J}[E_C + 2k_B T_e \mathcal{H}_0^1(\eta_e)] - \kappa_e \nabla T_e \ , \\ &\mathbf{W}_h = \mathbf{J}[-E_V + 2k_B T_h \mathcal{H}_0^1(\eta_h)] - \kappa_h \nabla T_h \ . \end{aligned} \tag{7}$$

Similarly for the lattice system the lattice current is given by

$$\mathbf{W}_{\rm lat} = -\kappa_{\rm lat} \nabla T_L \ , \tag{8}$$

where $\kappa_{\rm lat}$ is the lattice thermal conductivity. After photoexcitation, electrons and holes possess kinetic as well as

band-gap energy. Therefore one may express the total energy density for the electron (U_e) and hole (U_h) system of N carriers in the following way:

$$U_e = NE_C + \tfrac{3}{2}Nk_B T_e \mathcal{H}^{3/2}_{1/2}(\eta_e) ,$$
$$U_h = -NE_V + \tfrac{3}{2}Nk_B T_h \mathcal{H}^{3/2}_{1/2}(\eta_h) . \tag{9}$$

This completes the equations which govern carrier and thermal transport, assuming that the particles are in local thermodynamic equilibrium, and can be represented by spatially and temporally varying macroscopic parameters. Next we consider the continuity equations which dictate the dynamics of the macroscopic variables, N, T_e, T_h, and T_L:

$$\frac{\partial N}{\partial t} = -\nabla\cdot\mathbf{J} + \mathcal{G} + \mathcal{R}, \quad C_L\frac{\partial T_L}{\partial t} = -\nabla\cdot\mathbf{W}_{\text{lat}} + L_e + L_h ,$$
$$\frac{\partial U_e}{\partial t} = -\nabla\cdot\mathbf{W}_e + S_e - L_e - L_{e\to h} , \tag{10}$$
$$\frac{\partial U_h}{\partial t} = -\nabla\cdot\mathbf{W}_h + S_h - L_h + L_{e\to h} ,$$

where S_e and S_h represent the energy source terms for electrons and holes, L_e, L_h, and $L_{e\to h}$ are the energy transfer terms (between electrons and phonons, holes and phonons, and electrons and holes, respectively), C_L is the lattice thermal conductivity, $\mathcal{R}$ is the net recombination rate, and $\mathcal{G}$ is the carrier generation rate. The net recombination rate is given by $-\gamma N^3$, where γ is the Auger recombination coefficient. We consider for the generation rate

$$\mathcal{G}(z,t) = \frac{(1-R)\alpha I_0(t)e^{-\alpha z}}{\hbar\omega_0} . \tag{11}$$

R is the reflectivity of the optical excitation, $I_0(t)$ is the intensity, $\hbar\omega_0$ is the photon energy, and α is the one-photon absorption coefficient. From $\mathcal{G}$ the quantities Se and S_h, which are the energy generation ratio for electrons and holes, respectively, can be calculated using conservation of energy and momentum in the absorption process.

To this point, the derivation has been purposely kept in its most general form within the restrictions of the assumptions. In order to simplify the computational solution of the equations when the microscopic energy transfer terms are included below, the distribution functions are now simplified to be of a Maxwell-Boltzmann form. One simply replaces the factor $\mathcal{H}^i_j(\eta_c)$ by unity in the above equations. This approximation to the Fermi-Dirac distribution function is valid for the carrier densities and temperature considered in this paper.

The total energy-loss rate of the carriers is incorporated in the model through the use of analytic expressions for the various scattering mechanisms.[21–24] These include (1) intravalley acoustic phonons and optical phonons, (2) intervalley acoustic and optical phonons, and (3) electron-hole scattering.

The average energy-loss rate of a Maxwellian distribution of carriers of effective mass m^* to acoustic modes is given by

$$\left\langle \frac{dE}{dt} \right\rangle_{\text{ac}} = -\frac{8\sqrt{2}}{\pi^{3/2}} \frac{\varepsilon_{\text{ac}}^2 m^{*5/2}}{\hbar^4\rho}(k_B T_c)^{3/2}\left[1-\frac{T_L}{T_c}\right] , \tag{12}$$

where ε_{ac} is the appropriate acoustic deformation constant (see Table I), and ρ is the density of the semiconductor. Energy loss by hot carriers to acoustic modes is generally small compared with the loss due to optical phonons.

The energy-loss rate for a distribution of hot carriers due to intra-L-valley and intra-valence-band optical-phonon processes is obtained by integrating the corresponding optical-phonon generation rate[11] $(\partial n_{\text{q}}/\partial t)_{\text{gen}}$ over all wave vectors. The transverse or longitudinal optical-phonon generation rate for a Maxwellian distribution of free carriers is given by[11,21]

$$\left[\frac{\partial n_{\text{q}}}{\partial t}\right]_{\text{gen}} = \left[\frac{\pi}{2}\right]^{1/2} \frac{\mathcal{D}_c^2}{\rho\mathcal{E}_{\text{ph}}q}\left[\frac{m^*}{k_B T_c}\right]^{1/2} \times \frac{e^{x_0 - x/2} - e^{x/2}}{e^{x_0}-1}e^{x_1} , \tag{13}$$

where $x_0 = \mathcal{E}_{\text{ph}}/k_B T_L$, $x = \mathcal{E}_{\text{ph}}/k_B T_c$, $x_1 = -\hbar^2 x/2m^*(m^{*2}\mathcal{E}_{\text{ph}}/\hbar^4 q^2 + q^2/4\mathcal{E}_{\text{ph}})$, $\mathcal{D}_c$ is the optical deformation-potential constant, and $\mathcal{E}_{\text{ph}}$ is the optical-phonon energy. Multiplying this equation by $\mathcal{E}_{\text{ph}}$ and integrating it over all wave vectors gives for the energy relaxation rate due to a particular phonon branch,

$$\left\langle \frac{dE}{dt} \right\rangle_{\text{op}} = -\left[\frac{2}{\pi}\right]^{1/2} \frac{\mathcal{D}_c^2 m^{*3/2}}{\pi\hbar^2\rho}(k_B T_c)^{1/2} \times \frac{e^{x_0 - x} - 1}{e^{x_0}-1}\,\frac{x}{2}e^{x/2}\mathcal{K}_1(\tfrac{1}{2}x) , \tag{14}$$

where $\mathcal{K}_1$ is the modified Bessel function. Electron intervalley scattering may be treated much like the intravalley scattering by optical phonons.[21,23] The average rate of energy loss by a carrier due to intervalley scattering from valley i to valley j may be calculated using Eq. (14) with $\mathcal{D}_c$ replaced by $\mathcal{D}_{ij}$, $\mathcal{E}_{\text{ph}}$ with $\hbar\omega_{ij}$, and finally m^* with the density-of-state mass of the j valley, m_j^*.[21] Here $\mathcal{D}_{ij}$ and $\hbar\omega_{ij}$ are the intervalley deformation-potential constant and phonon energies associated with intervalley scattering, respectively. The terms L_e or L_h are found by summing the energy relaxation rates over the various phonon modes.

Electron-hole energy exchange, $L_{e\to h}$, was treated in the static screening limit, including only intra-heavy-hole transitions, to be consistent with the simplifying band-structure assumptions made above. Details of the computational technique used to evaluate the electron-hole energy exchange rate can be found elsewhere.[22] Although the Coulomb-mediated energy-loss rate of electrons in anisotropic conduction-band valleys is in general anisotropic, a single density-of-states effective mass was adopted and used in the isotropic calculation of Ref. 22. As will be shown below, the absolute value of the energy exchange rate between electrons and holes turns out not to strongly affect the calculated values of nonequilibrium phonon populations or the transient reflectivity. This process was included in the overall model merely to obtain an estimate of how strongly the electron and hole subsystems are coupled under the present experimental conditions.

For a direct comparison with the Raman experiments, we also calculate the temporal evolution of the optical-phonon population generated due to intra-L-valley and intra-heavy-hole valence-band relaxation processes. This involves solving a partial differential equation for the Raman-active phonon occupation number n_q at $\lambda=0.575$ μm

$$\frac{\partial n_q}{\partial t}=\left[\frac{\partial n_q}{\partial t}\right]_{\text{gen}}^{T}-\left[\frac{n_q-n_q^{\text{eq}}}{\tau}\right], \tag{15}$$

where n_q^{eq} is the equilibrium phonon occupation, T indicates the total contribution from relaxing electrons and holes, and τ is the nonequilibrium phonon decay time determined experimentally[11] to be 8 ± 1 ps at 77 K and 4 ± 1 ps at 300 K.

IV. RESULTS AND DISCUSSION

The remainder of this paper is devoted to comparing and discussing the calculated carrier and phonon dynamics with the experimental data. First, the equations in the preceding section which describe the evolution of electron temperature, hole temperature, carrier density, and optical-phonon population were solved using the material parameters listed in Table I, with an excitation term[11] corresponding to a Gaussian 4-ps (FWHM), $\lambda=0.575$ μm laser pulse of energy 0.7 nJ, focused to a spot of diameter 30 μm ($F=10^{-1}$ mJ/cm^2). The sample temperature is taken to be 77 K and the steady-state carrier density is taken to be 10^{16} cm^{-3}. The absorption depth[25] of optical pulses at this wavelength is 0.1 μm at 77 K and 0.04 μm at 300 K while the reflectivity R is ≈ 0.5. Appropriate boundary conditions were used to solve the equations, assuming negligible surface recombination and a sample thickness of 5 μm, a thickness which is large compared to carrier diffusion depths for time scales of interest.

Figure 1 shows theoretical results for the temporal evolution of N, T_e, T_h, and T_L at the surface of the sample. The simulations start at -10 ps and end at 20 ps with the peak of the pump pulse taken at $t=0$. The main features of the carrier density evolution are the fast rise time, which simply reflects the integrated profile of the incident Gaussian pulse, and the two distinct regimes in which the carrier density drops at different rates. After the carrier density reaches its peak value there is an initial rapid reduction which occurs only for a few picoseconds. This is followed by a much slower rate of density drop which persists for tens of picoseconds. The reduction of surface density is due to diffusion alone, since Auger recombination which is the dominant recombination mechanism is still negligibly slow (lifetime ~ 10 μsec at carrier density of 10^{18} cm^{-3}) at these densities and time scales. The fact that the rapid diffusion takes place only while the carrier temperatures remain well above the ambient temperature gives a clue as to the origin of the two regimes of diffusion. From the model we understand that the increase of carrier temperature causes the ambipolar diffusivity (see Fig. 2) to increase above the value corre-

TABLE I. Material parameters of germanium (Refs. 19 and 23).

Parameter	Value	Units
ρ	5.32	g/cm^3
m_Γ^*	0.04	m_0
m_L^*	0.22	m_0
m_Δ^*	0.32	m_0
D_e^0 (77 K)	583	cm^2/sec
D_h^0 (77 K)	232	cm^2/sec
D_e^0 (300 K)	103	cm^2/sec
D_h^0 (300 K)	54	cm^2/sec
γ	2	10^{-31} cm^6/sec
C_L	1.7	J K^{-1}cm^{-3}
$\varepsilon_{ac}(\Gamma)$	8.0	10^{-12} erg
$\varepsilon_{ac}(\Delta)$	14.4	10^{-12} erg
$\varepsilon_{ac}(L)$	17.6	10^{-12} erg
ε_{ac}(hole)	7.4	10^{-12} erg
$\mathcal{D}_e$	6.4	10^{-4} erg/cm
$\mathcal{D}_h$	14.0	10^{-4} erg/cm
$\mathcal{D}_{\Delta\Delta}^{(\text{inter})}$(LO)	15.2	10^{-4} erg/cm
$\mathcal{D}_{LL}^{(\text{inter})}$(LA,LO)	4.8	10^{-4} erg/cm
$\mathcal{D}_{L\Delta}^{(\text{inter})}$(LA)	6.6	10^{-4} erg/cm

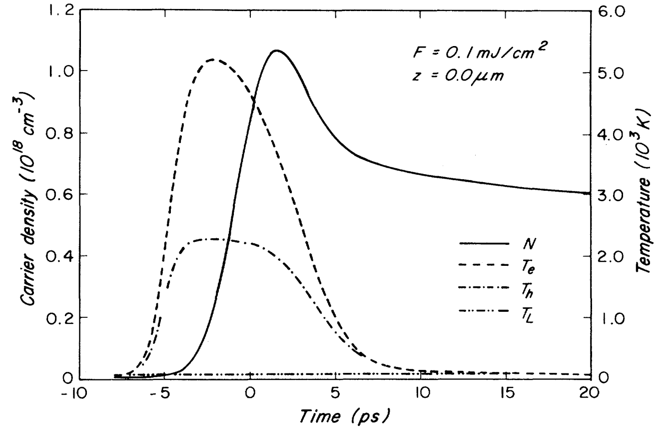

FIG. 1. Temporal evolution of the carrier density (N), electron (T_e), hole (T_h) and lattice (T_L) temperatures at the surface of Ge at 77 K for 0.1 mJ/cm^2, 4-ps pulse excitation. The rise in T_L is ≈ 0.5 K.

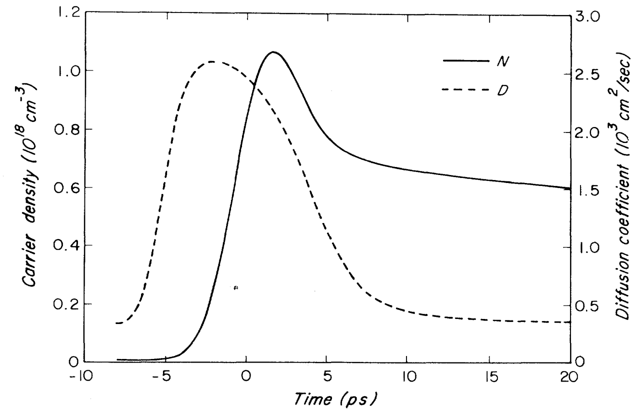

FIG. 2. Temporal evolution of carrier density (N), and ambipolar diffusion coefficient (dashed curve) corresponding to Fig. 1.

sponding to $T_e = T_L = 77$ K thereby forcing carriers to move out of the excitation region faster. When the temperature of the carriers reaches that of the lattice the diffusivity decreases to its equilibrium value and the carrier density decay rate is reduced. The density is in fact reduced below what it would be at the same time if a constant diffusion coefficient had been used, since by the time the diffusion coefficient drops to its ambient value the carrier density gradient is reduced.

The electron and hole temperatures increase during the early part of the pulse and reach maximum values at $t = -2$ ps. This maximum is reached before the peak of the pulse (as noted by van Driel[13]) because at very low densities the rate at which the optical pulse is increasing the kinetic energy of the carrier system is larger than the rate at which the heat capacity is increasing. The surface electron and hole temperatures peak at 5200 and at 2400 K, respectively, with both maxima occurring at approximately the same point in time, i.e., at $t = -2$ ps. The maximum values are consistent with ~1 eV of energy provided to each optically excited electron and ~0.3 eV to each hole.

The temperature for the holes has a plateau once it reaches a maximum value; this is due to the energy drawn from the electron system under *e-h* scattering. We have carried out simulations where this carrier-carrier scattering relaxation time $\tau_{e\text{-}h}$ was set equal to 0 and ∞. In the case where electrons and holes were viewed as decoupled systems ($\tau_{e\text{-}h} = \infty$) the simulation curves appear similar to those seen in Fig. 1. The most notable difference was observed in the time dependence of T_h. Under these conditions no plateau is observed, and once the peak value is reached, the hole temperature drops and reaches the lattice temperature at a time different from the time at which the electron temperature reaches the lattice temperature. In the opposite extreme where electrons and holes are strongly coupled ($\tau_{e\text{-}h} = 0$) they are forced to share a common temperature. The calculation of statically screened electron-hole energy transfer therefore suggests that under the present experimental conditions, the two carrier subsystems are essentially decoupled. Although the model calculations of the time-resolved reflectivity are not sensitive to details of the electron-hole energy exchange, the calculated nonequilibrium optical-phonon dynamics are. In particular, the good agreement between experiment and theory described below for the delay and absolute magnitudes of nonequilibrium phonon populations is obtained only if the electron-hole energy exchange is calculated explicitly, or if the two systems are assumed decoupled. A significant, 25% error in both the delay and peak magnitudes of the phonon population is made if the carriers are assumed to maintain a common temperature at all times.

In Fig. 3 we show the spatial profile of N, T_e, T_h, and T_L when T_e, T_h reach their maximum at $t = -2$ ps. The spatial decay depths reflect the diffusion dynamics. A significant result is the lack of variation of the carrier density over the absorption depth. The decay depth associated with the carrier temperatures is larger than that of the carrier density since heat can be transported not only through carrier diffusion but also through carrier col-

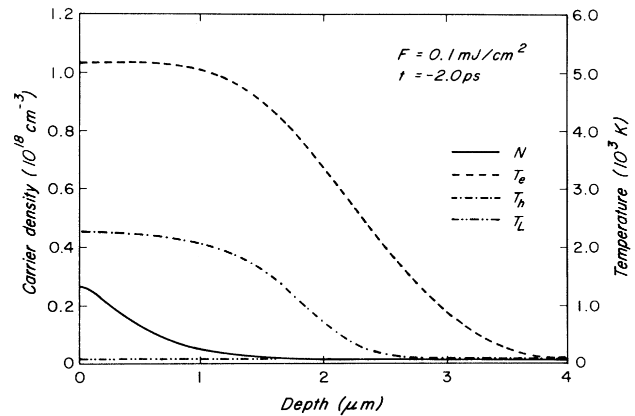

FIG. 3. Spatial evolution of the carrier density (N), electron (T_e), hole (T_h), and lattice (T_L) temperatures in Ge at 77 K corresponding to Fig. 1 at $t = -2$ ps.

lisions. To a good approximation one may consider a homogeneous carrier density over the absorption depth of the Raman and reflectivity probe pulses under the conditions employed in the experiments.

Our previously reported, time-resolved Raman studies of Ge showed that the nonequilibrium density of LO and TO phonons generated by the pump pulses were basically identical, as were their lifetimes.[11] Hence in our model we treat LO and TO phonons on an equal footing. The calculated temporal evolution of the nonequilbrium optical-phonon population of wave vector 1.2×10^6 cm^{-1}, at 77 and 300 K, is shown by the solid curves in Figs. 4 and 5. There is a fast rise time associated with phonon generation by cooling carriers and a slower decay due to the decay of the zone-center phonons into acoustic phonons. Also shown are the time-dependent optical-phonon populations deduced from the anti-Stokes Raman-scattering intensity.[11] The absolute values were obtained from calibrated Stokes/anti-Stokes ratios in the case of 77-K data, and from the ratio of nonequilibrium to equilibrium anti-Stokes scattering intensities for the 300-K data. The phonon lifetimes τ used to obtain the calculated curves were 8 and 4 ps for 77 and 300 K, respectively.

Note that the delay between the peak of the pump pulse ($t=0$) and the maximum nonequilibrium phonon occupation agree, while the absolute value of the nonequilibrium populations agree within a factor of 2. This agreement between experimental Raman data and the calculated result, with no variable fit parameters, is considered satisfying in two respects. First, the delay is a function of material parameters only, and is therefore insensitive to errors in estimating the precise excitation conditions. Second, the error in the absolute scale for the experimental nonequilibrium phonon population shown in Figs. 4 and 5 is ~±50%, due mainly to uncertainties in the precise sizes and the overlap of the pump and probe beams. Therefore even the absolute value of the excess occupation number is basically in agreement with the model within experimental error.

We note that the ratio of optical-phonon deformation potentials for holes to electrons used in the calculation[23]

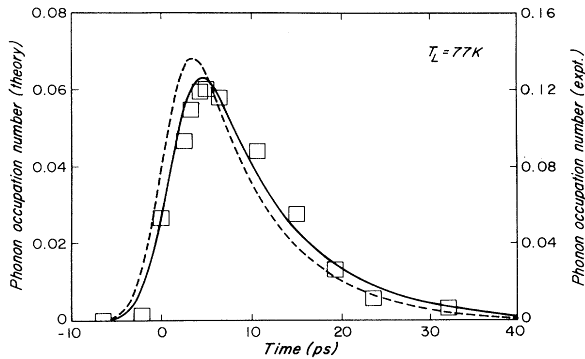

FIG. 4. Temporal evolution of the nonequilibrium optical-phonon population at 77 K corresponding to the excitation condition in Fig. 1. The squares represent experimental data, the solid and dashed curves are calculated using the model with $\mathcal{D}_h/\mathcal{D}_e = 2.2$ and 3.2, respectively.

is 2.2. If the value of 3.2 suggested by Conwell (1969) is used instead, with the same electron deformation potential, the calculation yields the dashed curve in Fig. 4. Clearly the agreement is not as good.

It is interesting that one is able to measure a significant nonequilibrium population of optical phonons in Ge using time-resolved Raman scattering in the visible region of the spectrum. The success of the same technique in III-V materials, such as GaAs, has often been attributed to the polar nature of the electron–LO-phonon interaction in these materials. It has been argued that the $1/q$ dependence of the interaction matrix element in polar materials forces all of the electron's kinetic energy to flow to the lattice through a very restricted range of LO phonon modes near the zone center, close to the wave vector probed by visible beams. In nonpolar materials such as Ge, the carrier-phonon matrix element is wave-vector independent and it is not clear, *a priori*, why significant nonequilibrium phonon populations may be observed. Using Eq. (13) we have calculated, at 77 K, the contribution from both relaxing holes and electrons to the population of different optical-phonon modes in the Brillouin zone (see Fig. 6). The first notable feature in Fig. 6 is that most of the optical phonons are generated by the hot holes, as one would expect from the values of the deformation-potential constant (see Table I). It is also clear that most of the deformation-potential interaction takes place at small wave vectors, very close to that sampled by the Raman probe, despite the fact that the matrix element is wave-vector independent. The restriction of energy flow preferentially through relatively small wave-vector phonons is due to the kinematic restrictions required by energy and momentum conservation imposed by the band structure. These purely kinematic constraints, together with the ability to maintain a well-defined LO phonon mode at carrier densities in excess of 1×10^{17} cm^{-3} (due to the lack of polar electron-phonon interactions), explains why significant nonequilibrium optical-phonon populations can be observed in Ge.

Perhaps the most sensitive and important component of the model is the carrier diffusion process. With the full temperature-dependent ambipolar diffusion coefficient included [Eq. (6)], the maximum carrier density achieved in the Raman experiments is estimated to be $\sim10^{18}$ cm^{-3} (see Fig. 1). At this density, Auger recombination, impact ionization, nonlinear absorption, and lattice heating are all negligible effects, thus confirming the claim above concerning the moderate level of excitation used in these experiments and justifying the use of Maxwell-Boltzmann statistics. However, if diffusion is ignored altogether (see Fig. 7), the peak surface carrier density and the nonequilibrium optical-phonon occupation numbers are a full order of magnitude larger, which is clearly inconsistent with the Raman data. If a constant (equilibrium) ambipolar diffusion coefficient is used, the difference between experimental and theoretical results is not as large; nevertheless there is still a significant difference compared to the results obtained using a temperature-dependent diffusion coefficient.

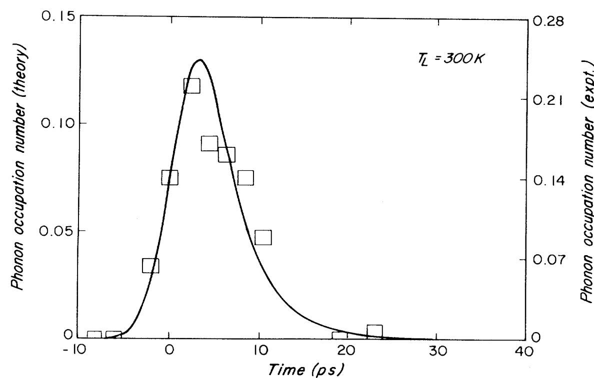

FIG. 5. Temporal evolution of the nonequilibrium optical-phonon occupation number at 300 K corresponding to the excitation condition in Fig. 1. The squares represent experimental data; the solid curve is calculated using the model with $\mathcal{D}_h/\mathcal{D}_e = 2.2$.

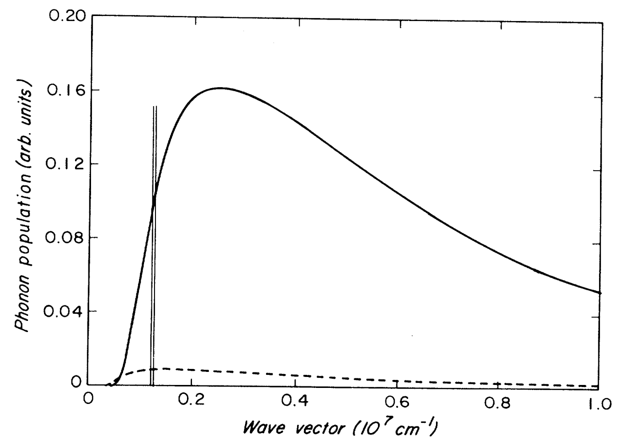

FIG. 6. Plot of the nonequilibrium LO phonon population at 77 K vs phonon wave vector, with the excitation condition in Fig. 1. The solid and dashed curves correspond to phonons generated from holes and electrons, respectively. The vertical lines mark the region probed by Raman backscattering.

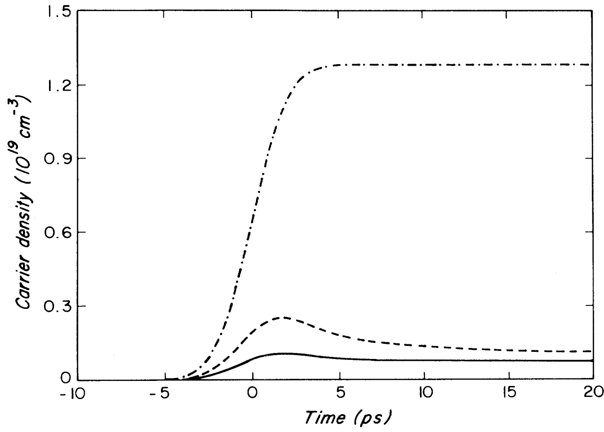

FIG. 7. Temporal evolution of the surface carrier density for different diffusion coefficients. The solid, dashed, and dash-dotted curves correspond to temperature-dependent, constant, and zero ambipolar diffusion coefficients, respectively.

Experimental data for the time-resolved reflectivity are shown in Fig. 8. The data reveal an initially fast decay in the reflectivity, followed by a much slower recovery towards the equilibrium value. The carrier density temporal profiles obtained from the simulations have features similar to those of the time-resolved reflectivity measurements. This suggested that a simple model of the optical properties with only a carrier density dependence, such as the Drude model, might be used to estimate the change in reflectivity.[26] However, a comparison of the reflectivity data and simulations using only the Drude model show that the small (<5 K) change in lattice temperature T_L might also be contributing to the reflectivity change. This effect was therefore also included in the reflectivity calculation using the time dependent T_L from the simulation.

At normal incidence the change in reflectivity due to changes in N and T_L is given by

$$\Delta R = \left| \frac{1-\sqrt{\epsilon+\Delta\epsilon_N+\Delta\epsilon_{T_L}}}{1+\sqrt{\epsilon+\Delta\epsilon_N+\Delta\epsilon_{T_L}}} \right|^2 - \left| \frac{1-\sqrt{\epsilon}}{1+\sqrt{\epsilon}} \right|^2 . \quad (16)$$

Here $\epsilon=(34+13i)$ is the equilibrium dielectric constant at $\lambda=0.575$ μm. In the Drude model we have

$$\Delta\epsilon_N = -\frac{4\pi e^2 N}{\epsilon_0} \left[\frac{1}{m_{\text{op}}^e} + \frac{1}{m_{\text{op}}^h} \right] \frac{1}{\omega^2 + i\omega/\tau_m} , \quad (17)$$

where m_{op}^e and m_{op}^h are the optical effective masses for the electrons and holes, respectively, ϵ_0 is the permittivity of the vacuum, and τ_m is the momentum relaxation time. For visible light $\omega \gg \tau_m^{-1}$ and we can neglect the imaginary contribution to $\Delta\epsilon_N$. The term $\Delta\epsilon_{T_L}$ is given by

$$\Delta\epsilon_{T_L} = \frac{\partial|\epsilon|}{\partial T_L}(T_L - 300 \text{ K}) ,$$

where we have estimated $\partial|\epsilon|/\partial T_L \approx 0.7\times10^{-2}$ K^{-1} at $\lambda=0.575$ μm by extrapolation of the temperature dependence of the reflectivity at nearby wavelengths.[27] Note, that without inclusion of $\Delta\epsilon_{T_L}$ the calculated value of $\Delta R/R$ agrees with the data for short times but is $\approx30\%$ lower than the data for delay times longer than 10 ps.

We used the above model to estimate the carrier density induced change in the reflectivity of the Ge at 300 K, in response to a 2-ps excitation pulse as described in Sec. II, for both constant and temperature-dependent diffusion. The results of these two calculations are shown in Fig. 8 along with the experimentally determined change in reflectivity. It is clear that the full temperature-dependent calculation yields a much better fit to the experimental results than does the calculation with a constant diffusion term. As with the phonon data, although more significance should be placed in the agreement with respect to shape than the absolute magnitudes both shapes and magnitudes are well accounted for by the model. Note that only the model with temperature-dependent diffusion can account for the short-term and long-term carrier density reduction. To obtain an acceptable signal-to-noise ratio, the fluence of the pump pulse used in the reflectivity experiments was more than an order of magnitude higher than in the Raman experiments. As a consequence, the peak carrier density achieved in the reflectivity experiment is $\sim1\times10^{19}$ cm^{-3}. It would of course be ideal if reflectivity and Raman data could be obtained under identical pump conditions, however this is not really necessary since even at these densities, no significant Auger recombination, lattice heating, or nonlinear absorption take place. The model results scale linearly over the range of densities spanned by the two experiments. The only deficiency of the model at the higher densities might be the assumption of Maxwell-Boltzmann carrier distributions, however the inclusion of Fermi-Dirac distributions is not expected to make a significant difference in the calculated reflectivity at these densities.

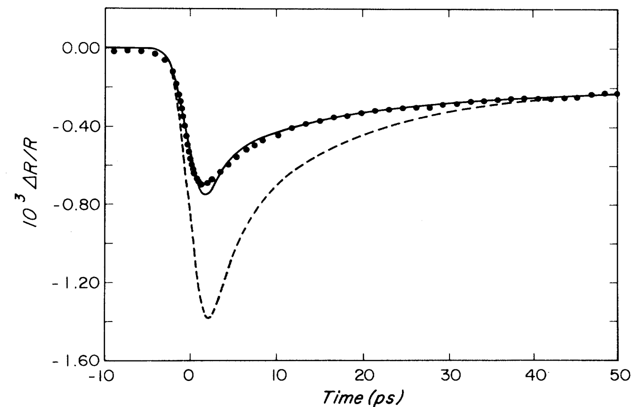

FIG. 8. Time-resolved reflectivity at 0.575 μm for $F=1$ mJ/cm^2 and $T_L=300$ K. The solid circles are experimental data, the solid and dashed curves are calculated reflectivity changes for the ambipolar diffusion coefficient assumed temperature dependent and constant, respectively.

V. SUMMARY

Through comparisons of picosecond Raman scattering and time-resolved reflectivity experiments with a kinetic model, we have demonstrated the ability of these techniques to probe subtle aspects of nonequilibrium carrier and phonon dynamics in Ge at moderate injected-carrier densities. In particular, nonequilibrium optical-phonon generation and hot-carrier diffusion processes can be quantitatively and self-consistently understood. We have also shown that the requirements of conservation of energy and momentum during carrier-phonon deformation potential interactions are sufficient to generate significant populations of Brillouin-zone-center optical phonons.

ACKNOWLEDGMENTS

H. M. van Driel and Andreas Othonos are grateful for support from the Natural Sciences and Engineering Research Council of Canada and the Ontario Laser and Lightwave Research Centre.

[1]S. A. Lyon, J. Lumin. **35**, 121 (1986).
[2]D. H. Auston, S. Mcafee, C. V. Shank, E. P. Ippen, and O. Teschke, Solid-State Electron. **21**, 147 (1978).
[3]D. von der Linde and R. Lambrich, Phys. Rev. Lett. **42**, 1090 (1979).
[4]P. C. Becker, H. L. Fragnito, C. H. B. Cruz, J. Shah, R. L. Fork, J. E. Cunningham, J. E. Henry, and C. V. Shank, Appl. Phys. Lett. **53**, 2089 (1988).
[5]F. W. Wise, I. A. Walmsley, and C. L. Tang, Appl. Phys. Lett. **51**, 605 (1987).
[6]J. Shah, B. Deveaud, T. C. Damen, W. T. Tsang, A. C. Gossard, and P. Lugli, Phys. Rev. Lett. **59**, 2222 (1987).
[7]H. Roskos, B. Rieck, A. Seilmeier, and W. Kaiser, Appl. Phys. Lett. **53**, 2406 (1988).
[8]D. von der Linde, J. Kuhl, and H. Klingenberg, Phys. Rev. Lett. **44**, 1505 (1980).
[9]J. C. Tsang, J. A. Kash, and S. S. Jha, Physica B+C **134B**, 184 (1985).
[10]J. A. Kash, J. C. Tsang, and J. M. Hvam, Phys. Rev. Lett. **54**, 2151 (1985).
[11]J. F. Young, K. Wan, and H. M. van Driel, Solid-State Electron. **31**, 455 (1988).
[12]J. F. Young, Kam Wan, A. J. Spring Thorpe, and P. Mandeville, Phys. Rev. B **36**, 1316 (1987).
[13]H. V. van Driel, Phys. Rev. B **19**, 5928 (1979).
[14]N. Potz and P. Kocevar, Phys. Rev. B **28**, 7040 (1983).
[15]D. C. Houghton, H. C. Liu, D. Landheer, M. Buchanan, and M. D'Iorio, SPIE J. **65**, 943 (1988).
[16]P. B. Corkum and R. S. Taylor, IEEE J. Quantum Electron. **QE-18**, 1962 (1982).
[17]H. M. van Driel, Phys. Rev. B **35**, 8166 (1986).
[18]A. Elci, M. O. Scully, A. L. Smirl, and J. C. Matter, Phys. Rev. B **16**, 191 (1977).
[19]M. Neuberger, *Group IV Semiconducting Materials,* Vol. 5 of *Handbook of Electronic Materials* (Plenum, New York, 1971); Landolt-Börnstein, *Numerical Data and Functional Relationships in Science and Technology* (Springer-Verlag, New York, 1982), Vols. 17 and 22.
[20]J. R. Drabble and H. J. Goldsmid, *Thermal Conduction in Semiconductors* (Pergamon, New York, 1961), p. 91.
[21]E. M. Conwell, *High Field Transport in Semiconductors* (Academic, New York, 1967), Suppl. 9.
[22]J. F. Young, P. J. Kelly, and N. L. Henry, Phys. Rev. B **36**, 4535 (1987).
[23]C. Jacoboni and L. Reggiani, Rev. Mod. Phys. **55**, 645 (1983).
[24]B. R. Nag, *Theory of Electrical Transport in Semiconductors* (Pergamon, Oxford, 1972).
[25]W. C. Dash and R. Newman, Phys. Rev. **99**, 1151 (1955).
[26]A. Othonos, H. M. van Driel, Jeff F. Young, and Paul J. Kelly, Solid-State Electron. **32**, 1573 (1989).
[27]G. E. Jellison, Jr., D. H. Lowndes, D. N. Mashburn, and R. F. Wood, Phys. Rev. B **34**, 2407 (1986); G. E. Jellison (private communication).